Spatial and temporal evolution of argon sparks

Sivanandan S. Harilal

Optical emission spectroscopic studies of laser-created argon sparks are carried out. Pulses of 532 nm and 8 ns from a frequency-doubled Nd:YAG laser are used to create an argon spark at 1 atm. Gated photography of 2 ns is used to investigate spark evolution at early times. Electron temperature and density measurements are made from the spectral data. The Stark broadening of emission lines is used to determine the electron density, and the Boltzmann plot of the singly ionized argon-line intensities is exploited for determination of the electron temperature. The dependence on electron temperature and density on different experimental parameters, such as distance from the focal point, delay time after the initiation of the spark, and laser energy, are discussed.

OCIS codes: 140.3440, 300.6550, 300.6500, 300.2140.

1. Introduction

There are several theoretical and experimental studies that explain how laser-created sparks come into existence and how they evolve.[1–7] There are two processes that may lead to creation of a laser spark due to focusing of an intense laser beam in a gas, namely, multiphoton ionization and cascade ionization. Cascade breakdown is the dominant mechanism at longer wavelengths ($\geq 1\ \mu m$) and moderate to high pressures when there are many electron–neutral collisions during the laser pulse.[8] Laser-produced sparks have many practical applications. Laser-induced sparks have been used as a source for producing high-intensity x rays[9] and extreme UV radiation in rare gases[10] and also for producing ultrafast shutters.[11] They are also capable of igniting gaseous mixtures or even of extinguishing a diffusion flame.[12] Apart from these applications, laser-created sparks can be used as a source for atomic emission spectrometry; in this case the technique is referred to as laser-induced breakdown spectrometry.[13,14] The spectrally and temporally resolved atomic emission with laser-induced breakdown spectrometry provides analytical information about the elemental composition of the sample. Recently this method has been used effectively for detecting airborne biological agents,[15] aerosols in ambient air,[16] and the equivalence ratio in combustion systems.[17]

The dynamics of laser-created sparks have been studied by various techniques, such as optical emission spectroscopy,[18,19] shadowgraphy,[20] interferometry,[20] and laser-induced fluorescence.[2] In published studies, however, little attention has been paid to the fundamental parameters of the plasma, such as electron temperature, electron density, and their evolution, especially at early times, after initiation of the laser spark. Several diagnostic techniques can be employed in determining temperature and density, including Thomson scattering, emission spectroscopy, Langmuir probe, and interferometry.[21–23] Thomson scattering is probably the most direct and least theory dependent, whereas spectroscopy is the simplest as far as instrumentation is concerned. Electron excitation temperatures and electron densities are estimated by using optical emission spectroscopy and are reported for laser-produced plasmas with solid targets[24,25] and gases such as air[26] and hydrogen.[27] Cadwell and Huwel[28] measured the temperature and density of laser-created argon sparks at delay times between 60 and 140 μs after spark formation. Tsuda *et al.*[29] reported the electron temperature of argon plasma created at high pressures (5–100 atm) and noted temperature increases with pressure.

In this paper we describe the spatial and the temporal analysis of laser-generated argon spark at 1 atm. Gated photography of 2 ns is used to investigate the spatial behavior of the spark kernel with time. Spatially and temporally resolved emission spectra are measured early in the plasma decay

The author is with the Center for Energy Research and the Department of Electrical and Computer Science Engineering, University of California San Diego, 9500 Gilman Drive, La Jolla, California 92093-0438 (e-mail, Harilal@fusion.ucsd.edu).

Received 25 August 2003; revised manuscript received 1 February 2004; accepted 30 March 2004.

0003-6935/04/193931-07$15.00/0

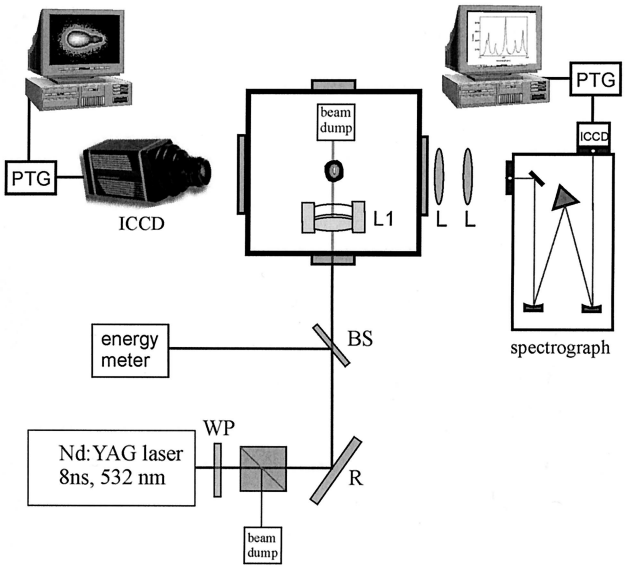

Fig. 1. Schematic of the experimental setup used for imaging and emission studies of argon spark: ICCD, intensified charged coupled device; PTG, programmable timing generator; WP, wave plate; R, reflector; BS, beam sampler; L_1, laser aplanet; L, lens.

(<600 ns). Emission spectra are used to infer the electron temperature T_e and density n_e of the spark. The Stark-broadening method is used for determining electron density, and the Boltzmann plot is used to elucidate the electron temperature by assuming the local thermodynamic equilibrium (LTE).

2. Experimental Setup

The schematic of the experimental setup is in Fig. 1. Pulses from a frequency-doubled Nd:YAG laser were used to create argon spark in a stainless-steel vacuum chamber. The chamber was evacuated and filled with argon gas at 1 atm. The laser provided clean temporal pulses with 8 ns FWHM with the help of an injection seeder (Fig. 2). The spatial structure of the laser profile was approximately Gaussian. The pulse energy was varied by the combination of a wave plate and a cube beam splitter. To create the breakdown plasma, the laser pulses were focused with an $f/5$ antireflection-coated laser aplanat (CVI Laser, LAP 75.0–15.0) with a focal length of 75 mm. The beam energy was monitored by an energy meter (Ophir Model 30A).

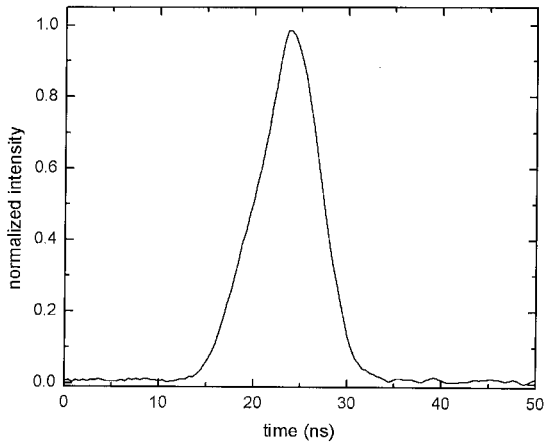

Fig. 2. Typical temporal profile of the laser pulse. The FWHM of the profile is ~8 ns. The profile is temporally cleaned by an injection seeder.

Plume imaging was accomplished with an intensified CCD (ICCD) camera (PI MAX Model 512 RB, 512×512 pixels) placed orthogonal to the laser beam. A Nikon lens was used to image the plume region onto the camera to form a two-dimensional image of the plume intensity. The visible radiation from the plasma was recorded integrally in a wavelength range of 350–900 nm. To keep 532-nm stray photons from reaching the camera, a magenta subtractive filter was used. A programmable timing generator was used to control the delay time between the laser pulse and the imaging system with an overall temporal resolution of 1 ns.

For space- and time-resolved spectroscopy an optical system was used to image the plasma plume onto the entrance slit of the spectrograph (Acton Pro, Spectra-Pro 500*i*) so as to have one-to-one correspondence with the sampled area of the spark and the image. The optical system was translated to monitor different parts of the spark. The spatial resolution provided by our optical system was better than 0.2 mm. The spectrograph was equipped with three gratings: 150, 600, and 2400 grooves/mm. The exit port of the spectrograph was coupled to an ICCD that was operated with vertical binning of the CCD array to obtain spectral intensities versus wavelength. The effective dispersion with 150, 600, and 2400 grooves/mm were 0.3, 0.07, and 0.012 nm/pixel, respectively. The recoded maximum resolution of the spectrograph with a 2400-grooves/mm grating with a He–Ne laser was ~0.025 nm.

3. Results and Discussion

The detailed structure of the focused laser beam in space and time is important in determining the beam energy required for breakdown. When a lens focuses the laser beam, the distribution of irradiance in the focal spot is determined by the mode structure in the laser oscillator, by the effect of amplifiers and apertures in the system, and by the parameters of the lens. The use of single-element lenses may lead to significant spherical aberration. The aberration may easily be minimized by a suitable choice of curvatures. The effect of spherical aberration on the distribution of irradiance in the focal region has been calculated by Evans and Morgan.[30] To avoid or minimize spherical aberration, we used a two-element laser aplanat for focusing the laser beam.

A. Spark Geometry

The time evolution of the plasma kernel is studied by using fast photography. Valuable information on the dynamics of the absorption of a laser beam and propagation of the gas-heating region is obtained by fast photography of the phenomenon. Time-resolved im-

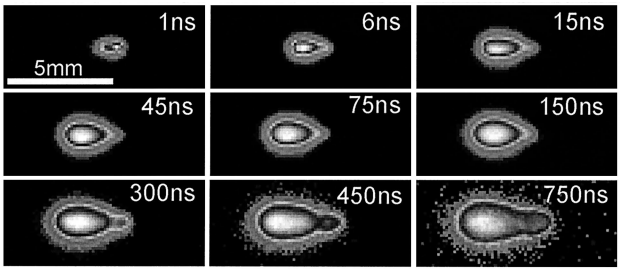

Fig. 3. Time evolution of visible emission from an argon spark recorded with an ICCD camera. The exposure time used was 2 ns. The laser energy used was 100 mJ, and background pressure was 1 atm. The timings in the images represent the time after the onset of spark formation. All the images are normalized to their maximum intensity. The smoothness of the sparks with time indicates the reproducibility.

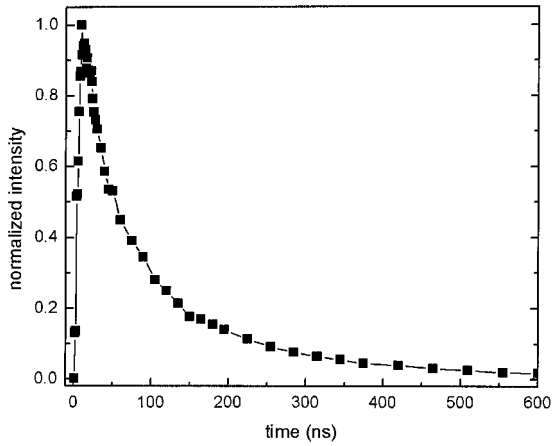

Fig. 4. Temporal evolution of the brightness taken from the images with time elapsed after the onset of spark. The spark emission peaked around 11 ns after the onset of plasma formation.

aging techniques could also provide details of the initial conditions of plasma.[31] The images are taken with the ICCD camera that views the plasma orthogonal to the laser-propagation direction. Figure 3 gives the evolution of an argon spark at 1 atm. The laser energy used is 100 mJ, and each image in the figure is recorded from an independent breakdown event and normalized to its maximum intensity. Timing jitter is less than 1 ns. The laser beam is incident from the left-hand side. The smoothness of the spark evolution attests to the reproducibility of the data.

The shapes of the argon spark at early times are spherical. At low energy levels the spark is confined very close to the focal volume. With increasing laser energy the kernel becomes more asymmetrical in shape; the backward plasma (toward the focusing lens) grows much faster than the forward plasma (away from the focusing lens). The layer of gas outside the plasma, although transparent to the laser beam, is heated by plasma radiation. This outside gas close to the plasma in turn becomes ionized to such an extent that it strongly absorbs the laser light. This layer is then heated further very rapidly and the temperature increases. By this time a new layer of plasma nearer the laser will have become strongly absorbing, so the boundary of the plasma will move toward the focusing lens. Hence the spark becomes optically thick and absorbs all radiation reaching the focal point. So the forward-moving component of the spark is absent at later times. The emission intensity of the spark is found to be higher at distances toward the focusing lens. The absorption of the laser photons by the plasma is mainly due to an inverse bremsstrahlung process. The time scale of this event is that of the laser pulse itself. For this work the incident laser irradiance is clearly greater than 1 GW cm^{-2}, and for those cases for which the absorbed energy significantly exceeds the breakdown threshold the plasma propagates as a laser-supported radiation wave.[5,26] The estimated velocity of argon spark propagation toward the focusing lens from the images is $\sim 1.4 \times 10^7$ cm/s. After the pulse ends the plasma continues to expand, although more slowly. Figure 4 represents the temporal evolution of the maximum brightness (taken from the images) of the argon spark with the time elapsed after the onset of the spark formation.

It is observed that the emission intensities increase rapidly to a certain time (11 ns) and then decrease with time. Then the spark emission decays over a period of a few microseconds. The time evolution of the spark at later times shows the dissipation times of the spark, ~5 ms.[4,32] It was also noticed that the shape of the sparks change significantly at later times.[4]

B. Spectroscopic Studies

The spectroscopic measurements are carried out to study the physical properties of the argon spark. Optical emission spectroscopic studies are made as a function of time and space at different laser energy levels. Time-resolved emission spectra are recorded at different locations in the spark. The typical emission spectra recorded at different times after the onset of the spark are given in Fig. 5. The spectra are recorded 2 mm from the focal point (toward the focusing lens) and with 100 mJ of laser energy. During the initial stages, especially <50 ns, the continuum emission dominates over line emission. The continuum radiation, or bremsstrahlung, occurs when a free electron collides with another particle and makes a transition to another free state of low energy, with the emission of a photon. In a spark that is sufficiently hot, most of the atoms are stripped of all their orbital electrons, and hence an electron–ion recombination and bremsstrahlung are the dominant emission mechanisms. As time evolves a large number of ionic and atomic transitions are superimposed on the continuum emission. We monitored the emission features early in the plasma decay (<600 ns). Radziemski *et al.*[33] well documented the emission features of the air plasma between 1 and 20 μs.

The plasma electron temperature was deduced

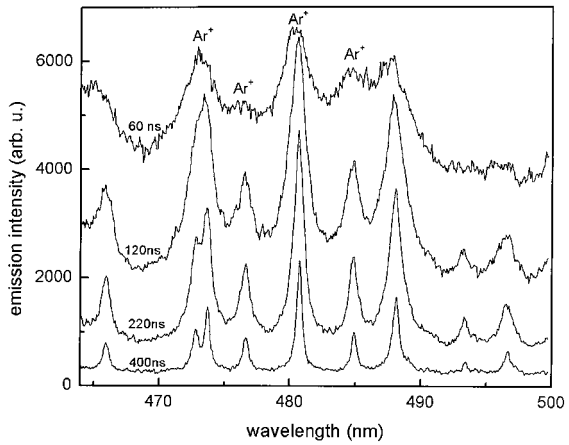

Fig. 5. Typical time-resolved emission spectra recorded after the onset of spark evolution. These spectra are recorded 2 mm away from the focal point in the backward direction. The gate of the intensifier was set at 10 ns. Emission lines used for the Boltzmann plot are also given.

from the Boltzmann plot method. If the plasma is assumed to be in the local thermodynamic equilibrium, the Boltzmann distribution can be used to estimate the population of the excited state, and it can be written as

$$n_{nm} = n_n \frac{g_m}{Z} \exp\left(-\frac{E_m}{kT}\right), \tag{1}$$

where n_{nm} is the population of the mth excited level, g_m is the statistical weight of the upper level of the transition, E_m is the excitation energy, k is the Boltzmann constant, and T is the temperature. The emission intensity of a line is related to the population of the excited level through

$$I_{nm} \approx A_{nm} n_{nm} \frac{hc}{\lambda_{nm}} = A_{nm} n_n \frac{g_m hc}{Z\lambda_{nm}} \exp\left(-\frac{E_m}{kT}\right), \tag{2}$$

where A_{nm} is the transition probability and λ_{nm} is the wavelength of the line. Hence, when the ratio of line intensities are used, the temperature can be estimated. We estimated the temperature by using the intensities of several Ar^+ lines. A plot of $\ln(I\lambda/Ag)$ against E for several spectral lines should be a straight line of slope $1/kT$. The use of multiple lines has the advantage of improving the accuracy of the temperature measurement as well as checking for errors in the line assignment or transition probability value. The designation and other spectroscopic constants used for determining the excitation temperature for argon spark are in Table 1. Transition probabilities A_{nm} and the statistical weights g_m of these lines are obtained from the literature.[34,35] A typical Boltzmann plot used for calculating the temperature is in Fig. 6.

One of the most powerful spectroscopic techniques for determining the electron density with reasonable accuracy is by the measurements of a Stark-broadened line profile of an isolated atom or singly charged ion. Stark broadening is the dominant broadening mechanism in laser-created sparks. In such a case the electron density can be deduced from the FWHM of a line. The FWHM of a Stark-broadened line (in angstroms) without ionic contribution is given by the simple relation[35]

$$\Delta\lambda_{1/2} = 2W\left(\frac{n_e}{10^{16}}\right)\text{Å}, \tag{3}$$

where W is the electron-impact parameter, which can be incorporated for different temperatures.[35] We have selected the line-broadened profile of the Ar^+ line at 480.6 nm for the electron-density measurements. The impact parameter of the line is obtained from Griem.[35] Apart from Stark, other broadening mechanisms such as resonance, Doppler, and instrument broadening can affect the broadening of an emission line.[24] The effect of resonance broadening is proportional to the ground-state number density and the transition oscillator strength. Doppler broadening, which is due to different Doppler shifts experienced by the species in different regions of the

Table 1. Spectroscopic Data of Ar^+ Lines Employed for Temperature Determination

Wavelength (nm)	Energy (eV) (Upper Level)	g (Upper Level)	Transition Probability A_{ij} (10^8 s^{-1})
385.1	19.97	4	0.387
392.6	24.28	4	1.4
404.3	21.40	4	0.406
407.2	21.50	6	0.58
410.4	22.70	4	1.3
472.7	19.76	4	0.588
476.5	19.87	4	0.64
480.6	19.22	6	0.78
484.8	19.30	2	0.849

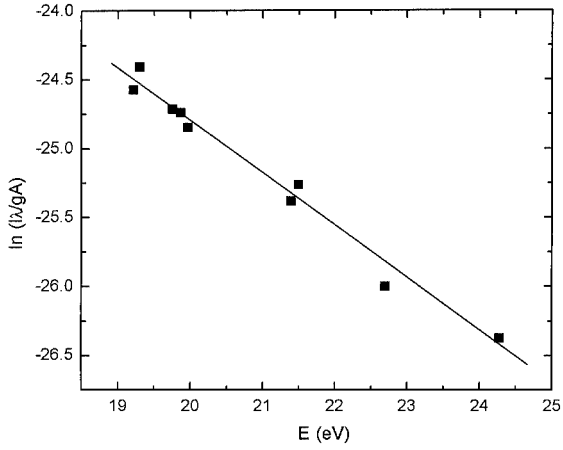

Fig. 6. Typical Boltzmann plot used for estimating temperature. The Intensities of Ar^+ lines are used, and other constants are in Table 1. The inverse slope of the best fit gives the temperature. This plot corresponds to time-integrated emission intensities recoded at the focal spot (laser energy, 100 mJ), which corresponds to a temperature of 2.25 ± 0.2 eV.

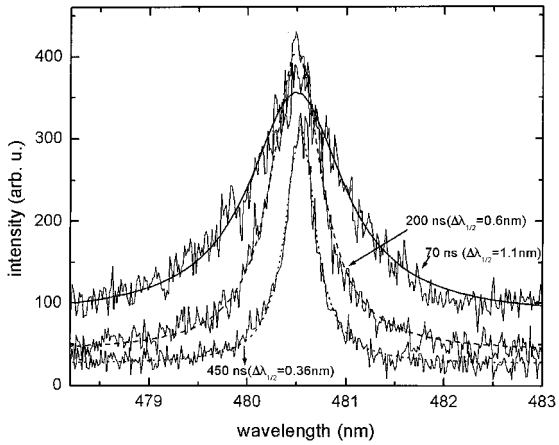

Fig. 7. Stark-broadened profile of Ar^+ transition at 480.6 nm at different times after the onset of spark. The FWHM of this line is used to infer electron density. The smooth curves represent the fitted Lorentzian curves. The measured Stark widths are also given.

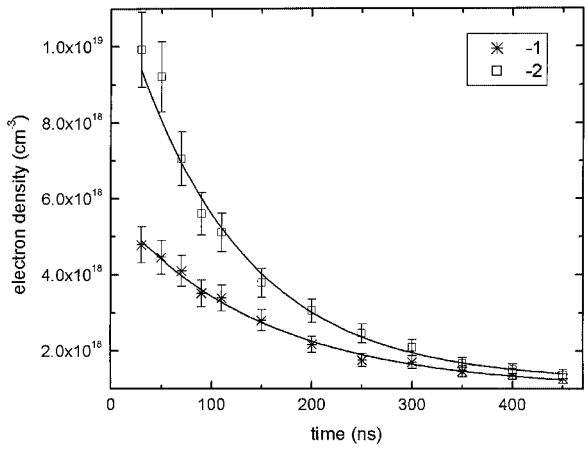

Fig. 9. Time evolution of density at different spatial points in the spark. Other experimental conditions are similar to Fig. 8.

plume with different velocity components, can also be ruled out in our experimental conditions because the spark expansion is slow after the end of the laser pulse. Setting the spectrograph at its maximum resolution can minimize the instrumental broadening. Typical Stark-broadened profiles of Ar^+ at 480.6-nm lines at different times after the onset of spark formation are given in Fig. 7. Stark-broadened line profiles are approximately Lorentzian, and the experimental results shown here in Fig. 7 fit fairly well with a typical Lorentzian profile.

We have measured the electron density and the temperature as functions of the axial distance from the focal point, the time after the onset of spark formation, and the laser energy. The temporal evolution of electron temperature and electron density is of prime importance, since many kinetic reaction rates depend directly or indirectly on these parameters.[25] The variation in temperature and density as a function of time is given in Fig. 8 and 9 for two axial points in the spark. Axial positions -1 and -2 correspond to 1- and 2-mm separation from the focal point and toward the focusing lens. At shorter times the line-to-continuum ratio is so small and the temperature measurement is sensitive to errors in setting the true continuum level. This problem is particularly acute for time are great as 50 ns. For times >50 ns the line-to-continuum ratios are within a reasonable limit, interference with the continuum measurement is not severe, and the values of n_e and T_e shown in Figs. 8 and 9 should be reliable. For these studies the gate width of the intensifier is set at 10 ns. An initial electron temperature of ~3 eV (35,000 K) and a density of 1×10^{19} cm^{-3} are observed at the -2 position. The density diminishes rapidly with time and then levels off at later times. Note that within 300 ns after the onset of spark formation the density drops to 2×10^{18} cm^{-3}. The fast decay rate can be attributed to plasma recombination. The density was found to be much lower at the -1 position, while the temperature did not vary much. This indicates that inverse bremsstrahlung is the most important absorption mechanism for spark propagation toward the focusing lens. Inverse bremsstrahlung strongly depends on density n_e^2 and weakly depends on temperature.[23] The electron temperature also drops with time but at a much slower rate than the density. Tsuda *et al.*[29] also observed a similar variation in electron temperature with time for an argon spark at high pressures (5–50 atm). Recently the temperature and density of laser-generated argon sparks have been estimated at delay times between 60 and 140 μs after the spark formation.[28] At these later times the estimated temperatures and densities varied from 9600 to 5600 K (0.83–0.5 eV) and 2.4 to 0.6×10^{16} cm^{-3}, respectively.

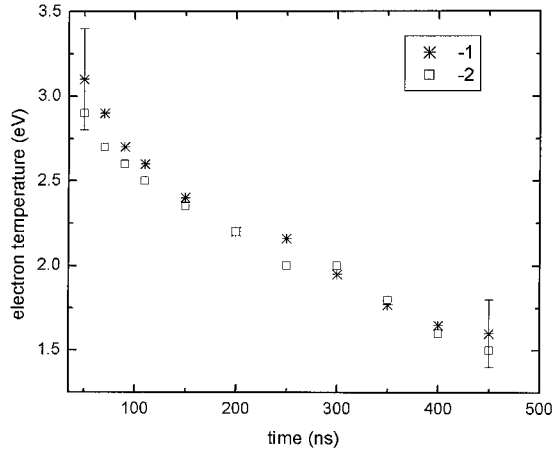

Fig. 8. Time evolution of electron temperature after the onset of spark formation. Positions -2 and -1, 2 and 1 mm toward the focusing lens from the focal point. The gate of the intensifier is set at 10 ns for these measurements.

The variation of temperature and electron density as a function of axial distance and for different laser energy levels is given in Fig. 10 and 11. Since both density and temperature rapidly change with time, these spectroscopic measurements are done in a time-

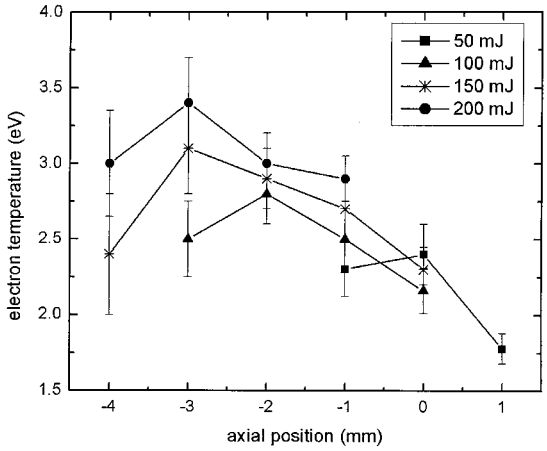

Fig. 10. Variation in temperature at different spatial points in the spark for various laser energies. All these measurements are done in a time-integrated manner. The delay and gate width are set at 50 and 500 ns, respectively. Axial position 0 corresponds to the focal point and the −ve and +ve numbers on the x-axis scale correspond to positions toward and away from the focusing lens.

integrated manner. For these studies the gate width and delay of the intensifier were set at 500 and 50 ns, respectively. Since time-integrated intensities were used for these estimations, the values of the temperature and density presented should be regarded as indicating the average conditions occurring in the spark, rather than as defining the conditions at a particular stage of its evolution. The temperature and density measurements at locations closer to the focal points show that their values are not much affected when we increase the laser energy. This indicates that increased energy of the laser pulse is used in plasma spatial growth and not in plasma heating. With increasing laser energy the spark propagates toward the laser beam. The spark becomes much hotter with the spatial positions toward the focusing lens. Similar to temperature, the density also increases initially with increasing separation from the focal position toward the focusing lens, which is characteristic of the inverse bremsstrahlung process. The rise in density depends also on the energy used for creation of the plasma.

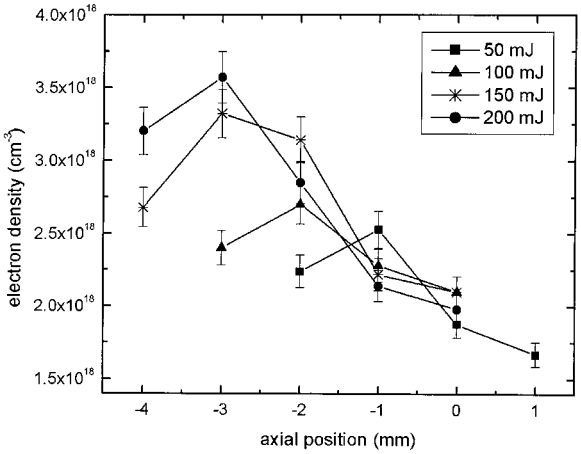

Fig. 11. Variation of density at different spatial points in the spark. The measurements are made in a time-integrated manner. All other experimental parameters are similar to Fig. 10.

Since we have assumed that the plasma is in a local thermodynamic equilibrium for our analysis of electron temperature, checking the minimum density condition for LTE is worth while[22]:

$$n_e \geq 1.4 \times 10^{14} T_e^{1/2} (\Delta E)^3 \mathrm{cm}^{-3}, \qquad (4)$$

where T_e and ΔE (the energy difference between upper and lower energy levels) are in electron volts. For the transition with the largest energy gap, $\Delta E = 3.2$ eV, and applied to a spark temperature of 3 eV, the criterion predicting the lowest limit for n_e is 8×10^{15} cm^{-3}. Our observed values of n_e are always greater than this limit, implying that the LTE approximation assumed for our analysis is valid.

4. Conclusions

The emission details of an argon spark at a 1-atm pressure have been investigated with 2-ns gated photography and optical emission spectroscopy. The laser-induced argon spark is created by focusing 8-ns pulses from a frequency-doubled Nd:YAG laser. Significant energy absorption and a cascade type of optical breakdown start with the generation of initial free electrons. Following the rapid growth of electron density, the initial plasma becomes optically thick and absorbs practically all incident energy in the latter portion of the laser pulse. Because of this, soon after the breakdown an apparent shift in the spark results from the buildup of a laser-supported radiation wave that travels against the incoming laser beam, whereas the opposite side obscured by the absorbing plasma is no longer fed by laser energy. The observed movement toward the laser beam ceases by the end of the laser pulse; at this stage the emission intensity reaches the maximum value, from which it decays in time, which is of the order of a few microseconds.

We performed a detailed measurement of electron density and temperature by using spectroscopic means. Line-intensity ratios of the same ionization stages of the argon employing Boltzmann plot have been used for determining electron temperature, and the Stark-broadened profile of the first ionized argon species is used for the electron-density measurements. The dependence of density and temperature on different experimental parameters, such as distance from the focal point, time after the onset of spark formation, and laser energy, is carried out. At earlier times the intense continuum radiation is dominated. The line-to-continuum ratio improves as time evolves. An initial temperature of ~3 eV (35000 K) and a density of 1×10^{19} cm^{-3} are measured. The density and temperature measurements also showed that their values increase with separation from the focal spot and toward the focusing lens. The temperature and density measurements at locations closer to the focal points indicate that their

values are not affected much by the increase in laser energy, which points out that the increased energy in the laser pulse is used in plasma spatial growth and not in plasma heating.

The author acknowledges C. V. Bindhu, Mark Tillack, A. Gaeris, and F. Najmabadi for technical help and support.

References

1. Y. L. Chen, J. W. L. Lewis, and C. Parigger, "Spatial and temporal profiles of pulsed laser-induced air plasma emissions," J. Quant. Spectrosc. Radiat. Transfer **67,** 91–103 (2000).
2. Y. L. Chen and J. W. L. Lewis, "Visualization of laser-induced breakdown and ignition," Opt. Exp. **9,** 360–372 (2001).
3. Y. Gamal, L. El-Nadi, M. O. Omara, B. Ghazoulin, and K. A. Sabour, "On the study of the electron kinetic processes in the breakdown of argon by 0.53-μm and 0.248-μm laser radiation," J. Phys. D **32,** 1633–1639 (1999).
4. M. Longenecker, L. Huwel, L. Cadwell, and D. Nassif, "Laser-generated spark morphology and temperature records from emission and Rayleigh scattering studies," Appl. Opt. **42,** 990–996 (2003).
5. L. J. Radziemski and D. A. Cremers, Laser Induced Plasmas and Applications (Marcel Dekker, New York, 1989).
6. G. V. Ostrovska and A. N. Zaidel, "Laser spark in gases," Sov. Phys. Usp. **16,** 834–855 (1974).
7. T. P. Hughes, Plasmas and Laser Light (Wiley, New York, 1975).
8. C. G. Morgan, "Laser-induced breakdown of gases," Rep. Prog. Phys. **38,** 621–665 (1975).
9. X. F. Wang, R. Fedosejevs, and G. D. Tsakiris, "Observation of Raman scattering and hard x rays in short pulse laser interaction with high density hydrogen gas," Opt. Commun. **146,** 363–370 (1998).
10. S. Kranzusch, C. Peth, and K. Mann, "Spatial characterization of extreme ultraviolet plasmas generated by laser excitation of xenon gas targets," Rev. Sci. Instrum. **74,** 969–974 (2003).
11. L. J. Dhareshwar, P. A. Naik, and D. D. Bhawalkar, "A plasma shutter to generate a synchronized subnanosecond pulse for optical probing of laser-produced plasmas," Rev. Sci. Instrum. **62,** 369–375 (1991).
12. T. X. Phuoc, C. M. White, and D. H. McNeill, "Laser spark ignition of a jet diffusion flame," Opt. Laser Eng. **38,** 217–232 (2002).
13. D. A. Rusak, B. C. Castle, B. W. Smith, and J. D. Winefordner, "Fundamentals and applications of laser-induced breakdown spectroscopy," Crit. Rev. Anal. Chem. **27,** 257–290 (1997).
14. J. Sneddon and Y. I. Lee, "Novel and recent applications of elemental determination by laser-induced breakdown spectrometry," Anal. Lett. **32,** 2143–2162 (1999).
15. J. D. Hybl, G. A. Lithgow, and S. G. Buckley, "Laser-induced breakdown spectroscopy detection and classification of biological aerosols," Appl. Spectrosc. **57,** 1207–1215 (2003).
16. J. E. Carranza, B. T. Fisher, G. D. Yoder, and D. W. Hahn, "On-line analysis of ambient air aerosols using laser-induced breakdown spectroscopy," Spectrochim. Acta Part B **56,** 851–864 (2001).
17. F. Ferioli, P. V. Puzinauskas, and S. G. Buckley, "Laser-induced breakdown spectroscopy for on-line engine equivalence ratio measurements," Appl. Spectrosc. **57,** 1183–1189 (2003).
18. D. S. Jebens, H. S. Lakkaraju, C. P. McKay, and W. J. Borucki, "Time-resolved simulation of lightning by LIP," Geophys. Res. Lett. **19,** 273–276 (1992).
19. J. B. Simeonsson and A. W. Miziolek, "Time-resolved emission studies of Arf-laser-produced microplasmas," Appl. Opt. **32,** 939–947 (1993).
20. M. Villagran-Muniz, H. Sobral, R. Navarro-Gonzalez, P. F. Velazquez, and A. C. Raga, "Experimental simulation of lightning, interacting explosions, and astrophysical jets with pulsed lasers," Plasma Phys. Controlled Fusion **45,** 571–584 (2003).
21. S. Amoruso, R. Bruzzese, N. Spinelli, and R. Velotta, "Characterization of laser-ablation plasmas," J. Phys. B **32,** R131–R172 (1999).
22. G. Bekefi, Principles of Laser Plasmas (Wiley-Interscience, New York, 1976).
23. H. R. Griem, Principles of Plasma Spectroscopy (Cambridge University, New York, 1997).
24. S. S. Harilal, C. V. Bindhu, R. C. Issac, V. P. N. Nampoori, and C. P. G. Vallabhan, "Electron density and temperature measurements in a laser-produced carbon plasma," J. Appl. Phys. **82,** 2140–2146 (1997).
25. S. S. Harilal, C. V. Bindhu, V. P. N. Nampoori, and C. P. G. Vallabhan, "Time evolution of the electron density and temperature in laser-produced plasmas from $YBa_2Cu_3O_7$," Appl. Phys. B **66,** 633–638 (1998).
26. S. Yalcin, D. R. Crosley, G. P. Smith, and G. W. Faqis, "Influence of ambient conditions on the laser air spark," Appl. Phys. B **68,** 121–130 (1999).
27. C. Parigger, D. H. Plemmons, and J. W. L. Lewis, "Spatially and temporally resolved electron number density—measurements in a decaying laser-induced plasma using hydrogen α-profiles," Appl. Opt. **34,** 3325–3330 (1995).
28. L. Cadwell and L. Huwel, "Time-resolved emission spectroscopy in laser-generated argon plasmas—determination of Stark broadening parameters," J. Quant. Spectrosc. Radiat Transfer **83,** 579–598 (2004).
29. N. Tsuda, Y. Uchida, and J. Yamada, "Spectroscopic measurement of high-pressure argon plasma produced by excimer laser," J. J. Appl. Phys. Part 1 **36,** 4690–4694 (1997).
30. L. R. Evans and C. G. Morgan, "Lens aberration effects in optical-frequency breakdown of gases," Phys. Rev. Lett. **22,** 1099–1102 (1969).
31. S. S. Harilal, C. V. Bindhu, V. P. Shevelko, and H. J. Kunze, "Charge-exchange collisions in interpenetrating laser-produced magnesium plasmas," Laser Part. Beams **19,** 99–103 (2001).
32. T. A. Spiglanin, A. McIlroy, E. W. Fournier, R. B. Cohen, and J. A. Syage, "Time-resolved imaging of flame kernels—laser spark ignition of H_2O–Ar mixtures," Combust. Flame **102,** 310–328 (1995).
33. L. J. Radziemski, T. R. Loree, D. A. Cremers, and N. M. Hoffman, "Time-resolved laser-induced breakdown spectrometry of aerosols," Anal. Chem. **55,** 1246–1252 (1983).
34. NIST Atomic Spectra Database, http://physics.nist.gov.
35. H. R. Griem, *Plasma Spectroscopy* (McGraw-Hill, New York, 1964).